RSC Advances

PAPER

View Article Online
View Journal | View Issue

Cite this: *RSC Adv.*, 2023, **13**, 30491

Synthesis of multifunctional amorphous metallic shell on crystalline metallic nanoparticles

Abhinav Parakh,†[ab] Mehrdad Toussi Kiani,†[ac] Emily Lindgren,[ad] Anabelle Colmenares,[e] Andrew Curtis Lee,[a] Yuri Suzuki[df] and Xun Wendy Gu*[e]

Colloidal nanoparticles can be coated with a conformal shell to form multifunctional nanoparticles. For instance, plasmonic, magnetic, and catalytic properties, chemical stability and biocompatibility can be mixed and matched. Here, a facile synthesis for depositing metal boride amorphous coatings on colloidal metallic nanocrystals is introduced. The synthesis is independent of core size, shape, and composition. We have found that the shell synthesis is limited to nanoparticles capped with short molecular weight and low binding energy ligands, and does not work with polyvinylpyrrolidone (PVP)-coated Ag nanoparticles or thiol-coated Au nanoparticles. Shell thickness can be as thin as 3 nm with no apparent pinholes. High pressure studies show that the coatings are highly resistant to crystallization and are strongly bonded to the crystalline core. By choosing either CoB or NiB for the coating, the composite nanoparticles can be either ferromagnetic or paramagnetic at room temperature, respectively.

Received 7th September 2023
Accepted 25th September 2023

DOI: 10.1039/d3ra06093d

rsc.li/rsc-advances

Metallic nanoparticles possess unique catalytic, electronic, optical, and magnetic properties.[1] Coating a secondary material on a nanoparticle core (*e.g.* to form a core@shell nanoparticle) can result in a combination of these properties, and introduce biocompatibility and environmental stability to the bare core.[2,3] Core@shell nanoparticles can have either crystalline or amorphous shells. While crystalline shells can be deposited on metallic cores to form nanoparticles such as Au@Ag,[4] this remains challenging due to lattice mismatch,[5] etching of the core due to shell electrochemical potential,[6] and restricted chemical synthesis routes. In contrast, amorphous carbon and silica shells are more compatible with different metallic cores. Yet, carbon shell coatings generally require complicated synthesis routes which involve high temperature pyrolysis.[7,8] Silica shell coatings have a facile aqueous phase chemical synthesis which is compatible with a wide variety of nanoparticle cores.[7] However, silica shell coatings add limited functionality to the nanoparticle core as silica is chemically inert, electrically insulating, and magnetic and optically inactive.

Metallic glasses (MGs) are similar to silica in terms of their amorphous atomistic structure, chemical stability, and corrosion resistance,[9,10] but have additional functionalities. Transition (Co/Ni/Fe) metal borides (TMBs) form MGs at 15–30 at% boron and are a viable alternative to silica shell coatings for nanoparticles. TMBs have been extensively explored as an economical alternative to noble metals for electrochemical water splitting,[11–14] as catalyst supports, and for hydrogen generation from borohydrides.[15–18] Coating noble metal nanoparticles with TMB can reduce the catalytic activity however, provide benefits like lowering the wt% of noble metal in the catalyst and extending the lifetime of noble metal nanoparticles. TMBs are electrically conductive,[19] chemically active,[11] and have favorable mechanical[20,21,22] and magnetic[23] properties which make them ideal candidates as multifunctional nanoparticle shells.

TMB nanoparticles have shown promise in nanomedicine as multifunctional components of radiation therapy and theranostics. Both FeB[24] and NiB[25] nanoparticles have low cytotoxicity with a half maximal inhibitory concentration of 82 mg mL^{-1} for pulmonary alveolar cells.[25] In addition, TMBs degrade at physiologically relevant pH levels measured in lysosomes and thus should not accumulate in the body.[24] Due to their magnetic properties, TMBs can be simultaneously used as contrast agents in magnetic resonance imaging (MRI) and as a cancer treatment *via* magnetic hyperthermia.[24] Amorphous NiB-coated Au nanocubes were shown to provide superior radiation tolerance when compared to silica, which makes them promising coatings for nanoparticle-enhanced radiation therapy[26] and as delivery

[a]*Department of Materials Science and Engineering, Stanford University, Stanford, CA 94305, USA*

[b]*Materials Engineering Division, Lawrence Livermore National Laboratory, Livermore, CA 94550, USA*

[c]*Department of Materials Science and Engineering, Cornell University, Ithaca, NY 14850, USA*

[d]*Geballe Laboratory for Advanced Materials, Stanford University, Stanford, CA 94305, USA*

[e]*Department of Mechanical Engineering, Stanford University, Stanford, CA 94305, USA. E-mail: xwgu@stanford.edu*

[f]*Department of Applied Physics, Stanford University, Stanford, CA 94305, USA*

† Equal contribution.

vehicles for the non-radioactive isotope ^{10}B for neutron capture therapy.[25] The combination of these properties with a plasmonic core could enable multimodal imaging such as surface enhanced Raman and MRI.[27]

Here, we describe the aqueous phase synthesis of NiB and CoB MG shells on metal nanocrystals and demonstrate that the synthesis approach is rapid and independent of core shape and size. Au and Pt cores are coated with NiB and CoB shells and their mechanical stability, optical behavior, and magnetic properties are investigated. The particles are also extremely stable and can withstand more than 55 GPa of hydrostatic pressure *via* a diamond anvil cell (DAC) without crystallization. NiB-coated Au nanoparticles retained the plasmonic properties of the Au core. NiB and CoB coated Au nanoparticles display super-paramagnetic and ferromagnetic behavior, respectively.

Methods

Nanoparticle synthesis

Au cores. Au nanoparticle cores were synthesized using two established methods.[28,29] Citrate stabilized Au nanoparticles (citrate-Au) were synthesized using the Bastús *et al.* method.[29] Briefly, 2.2 mM sodium citrate was dissolved in 150 mL deionized (DI) water and heated under vigorous stirring for 15 min with a condenser. After a temperature of 100 °C was reached, 1 mL of $HAuCl_4$ (25 mM) was added to the solution. Immediately after this, the reaction was brought to 90 °C and 1 mL of sodium citrate (60 mM) and 1 mL of $HAuCl_4$ solution (25 mM) were injected one after the other with 2 minutes between the injections. This process was repeated twice to make nanoparticles of the appropriate size. The nanoparticles were precipitated at 10 000 rpm centrifugation and then washed twice with water before dispersion in water.

Cetyltrimethylammonium chloride (CTAC) coated Au nanoparticles (CTAC-Au) were synthesized according to the Zheng *et al.* method.[28] 0.1 mL of 0.3 M $NaBH_4$ was rapidly added to a 5 mL solution of 0.25×10^{-3} M $HAuCl_4$ and 0.1 M CTAC. After 3 hours, 20 μL of the solution was added to an aqueous solution composed of 4 mL of 0.2 M CTAC and 3 mL of 0.1 M ascorbic acid. 200 μL of 0.01 M $HAuCl_4$ was then rapidly injected and stirred for 20 minutes. The solution was then cleaned twice in water at 10 000 rpm before redispersion in water at a concentration with a peak absorbance of 0.5 au.

Pt cores. 5 nm and 20 nm Pt nanoparticles were synthesized using the Bigall *et al.* method.[30] For 5 nm Pt nanoparticles, 18 mL of chloroplatinic acid hexahydrate (0.2%) was added to 232 mL of DI water at 100 °C. After 1 min, 5.5 mL of a solution containing sodium citrate (0.1%) and citric acid (0.05%) was added. Then 2.75 mL of $NaBH_4$ (0.08%), sodium citrate (1%), and citric acid (0.05%) was injected and the reaction was allowed to proceed for 10 min before cooling. The same solution was used without cleaning for shell coatings. For 20 nm Pt nanoparticles, 1 mL of 5 nm Pt nanoparticles were dispersed in 29 mL of DI water. 0.045 mL of chloroplatinic acid solution (0.4 M) was added to the solution. Then, 0.5 mL of sodium citrate (1%) and L-ascorbic acid (1.25%) was added. Temperature was increased to the boiling point while stirring. The nanoparticle solution was kept at 100 °C for 30 min, after which the nanoparticles were centrifuged at 10 000 rpm and cleaned with water before redispersion in water.

MG shell coating. Similar procedures were used to coat Au and Pt core particles with NiB or CoB. Here, we provide details for forming a 30 nm NiB shell on citrate–Au nanoparticles. 100 mL of DI water with 0.01 M sodium dodecyl sulfate and 0.001 M nickel nitrate hexahydrate (or cobalt nitrate hexahydrate for CoB shell coatings) was first prepared. Citrate–Au nanoparticle solution was added and then stirred rapidly before 0.02 g of $NaBH_4$ was dropped directly into the solution. After waiting for one minute for the solution to turn black, 1 mL of methanol with 0.01 M oleic acid was rapidly injected into the solution. The solution was left unstirred for one hour before centrifugation, cleaning, and dispersion in water. To make coatings of different thicknesses, the Au NP solution amount was varied. This synthesis could be scaled up from 10 mL to 200 mL batches by maintaining the same Au core concentration. For long term storage of particles, an additional 100 μL of methanol with 0.01 M oleic acid was added after cleaning. Samples are named as citrate-Au@NiB which indicates that citrate–Au nanoparticles were coated with NiB shell.

Characterization

TEM and STEM were performed using an FEI Tecnai G2 F20 X-TWIN at 200 kV. UV-vis absorbance spectrum was collected with an Ocean Optics spectrometer. For magnetic studies, CTAC-Au@NiB and CTAC-Au@CoB particles were massed using a microbalance and dried on a Si wafer. The Si wafer with the dried nanoparticles was loaded into a straw for bulk magnetometry measurement. The magnetic response of the nanoparticles was measured by SQUID Magnetometry, using a Quantum Design Evercool Magnetic Property Measurement System with the Reciprocating Sample Option (RSO). A Mao-type symmetric diamond anvil cell was used to conduct high pressure experiments. The diamond culet was 300 μm in size and Re gasket with 150 μm hole was used as the sample chamber. The sample was dried out on a silicon wafer and then a small piece of the sample was loaded into diamond anvil cell using a needle. Ruby was used as a pressure calibrant.[31] Neon gas was loaded as the pressure medium for quasi-hydrostatic measurements. *In situ* X-ray diffraction experiments were conducted at the Advanced Photon Source, Argonne National Lab beamline 16-BMD. An X-ray beam with a wavelength of 0.2952 Å and Mar image plate detector with an exposure time of 300 s were used for diffraction. For ambient pressure X-ray diffraction, the dried sample was transferred onto a 30 μm thick Kapton tape. Kapton tape background scattering was subtracted from the sample diffraction data. Radial integration was performed using the software DIOPTAS[32] and peak fitting was performed using a combination of Gaussian and Lorentzian peak profiles for further analysis.

Results and discussions

NiB shells with tunable thickness were deposited on citrate- and CTAC-Au nanoparticles (Fig. 1). In Fig. 1a, all particles have an

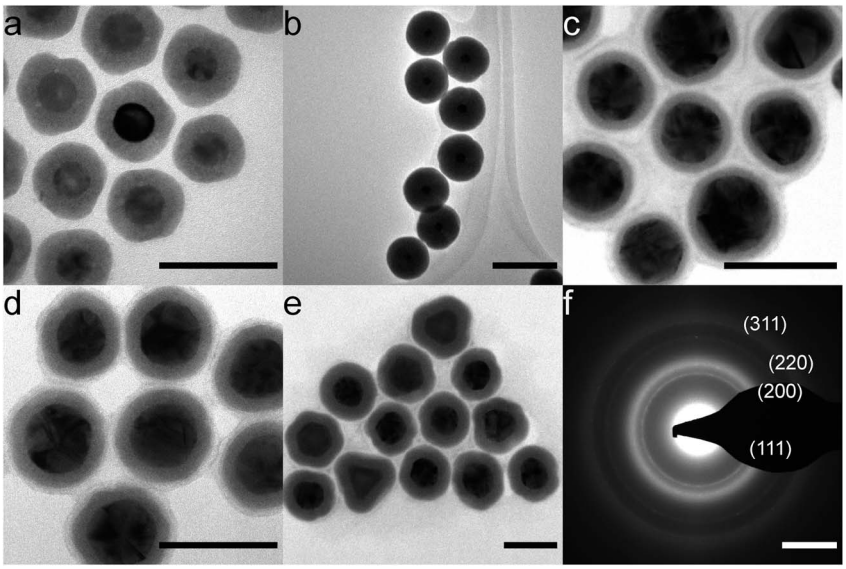

Fig. 1 CTAC-Au@NiB with (a) 8 nm coating and (b) 30 nm coating. Citrate-Au@NiB with (c) 3 nm, (d) 6 nm, and (e) 10 nm coating. (f) Selective area electron diffraction pattern of (e). Scale bar is 50 nm for (a, c–e), 100 nm for (b), and 4 nm^{-1} for (f).

approximately 8 nm thick coating. Thicker coatings of up to 30 nm, as shown in Fig. 1b, can be made by decreasing the initial Au nanoparticle concentration. For thicker coatings, some smaller NiB nanoparticles (<15 nm) nucleate in solution but can be removed using size selective centrifugal precipitation. Particles show a distinct boundary between the core and the shell, indicating that there is no diffusion. We have previously shown that Au nanocubes can also be coated in a similar manner.[26] The presence of boron in the NiB structure has been observed by inductively coupled plasma optical emission spectrometry (ICP-OES) and X-ray photoelectron spectroscopy (XPS) in our previous study[20] and by others.[23,33–41] The current synthesis strategy for NiB shell synthesis is similar to these previous studies indicating the presence of boron in the shell. In addition, several simulations of amorphous NiB structures have accounted for 19–35% boron content.[42–47]

The coating is also independent of defects in the core as citrate–Au core nanoparticles, which have numerous defects, showed similar conformal coatings (Fig. 1c–e). TEM diffraction of the 10 nm thick-coated particles in Fig. 1e showed the presence of (111), (200), (220) and (311) Au diffraction peaks and a broad amorphous ring (Fig. 1f). The coatings were conformal and pinhole free down to 3 nm shell thickness, which is comparable to silica coatings.[48,49]

The synthesis can be extended to other amorphous shells and crystalline cores. Citrate–Au NPs were coated with CoB using a similar synthesis method to NiB coatings (Fig. 2a). Citrate-Au@CoB particles have a larger variability in shell thickness compared to citrate-Au@NiB since the particles are not as stable in solution. Small, 5 nm Pt nanoparticles were coated with NiB using the same method (Fig. 2b). While the Pt nanoparticles are not a uniform shape and the final shapes vary, the coating thickness is relatively uniform. Fig. 2c the TEM diffraction pattern for the Pt@NiB nanoparticles with 5 nm core. We only observed (111) diffraction ring for the 5 nm core Pt@NiB due to the limited crystallite size. Coatings on larger, 20 nm Pt nanoparticles show a distinct microstructure in TEM images, where lines of contrast begin at the core and extend to the surface (Fig. 2d). These lines of contrast are thought to arise due to the non-epitaxial and cluster-driven growth from the surface.[33,50] Growth occurs from multiple nucleation sites on the Pt surface. The lines of contrast indicate the interfaces between two amorphous regions. STEM-EDS line mapping in Fig. 2d and e indicates a distinct boundary between the shell and core with no Pt diffusion in the shell.

The growth mechanism of the coating is dependent on the timing of adding oleic acid to the solution. If the methanol/oleic acid solution is added before $NaBH_4$ reduction, then homogenous nucleation occurs and NiB nanoparticles will form without coating the core nanoparticles in solution. The lack of oleic acid in solution during $NaBH_4$ reduction appears to increase the energy of homogenous nucleation, thereby promoting heterogenous nucleation on crystalline nanoparticles. By adding oleic acid one minute after $NaBH_4$ reduction, nucleation on the core nanoparticles first occurs, after which the oleic acid binds to the surface to enhance stability. Longer wait times before adding oleic acid (>5 minutes) led to dissolution of the shell as the MG shell is not stable in solution without oleic acid. The capping ligand on the core of the nanoparticle also plays a role in the nucleation of the MG shell on the surface of the core. Long polymeric ligands like polyvinyl pyrrolidone, commonly used in Ag nanoparticle synthesis, do not allow for the MG shell to nucleate on the core surface. Ionic and easily removable ligands like citrate and CTAC coated nanoparticles are ideal for MG shell nucleation.

Fig. 3c shows the XRD data for citrate-Au@NiB core–shell nanoparticle and NiB nanoparticles. Peak fitting showed that the first amorphous peak occurs at a q-spacing of 3.08 $Å^{-1}$ for

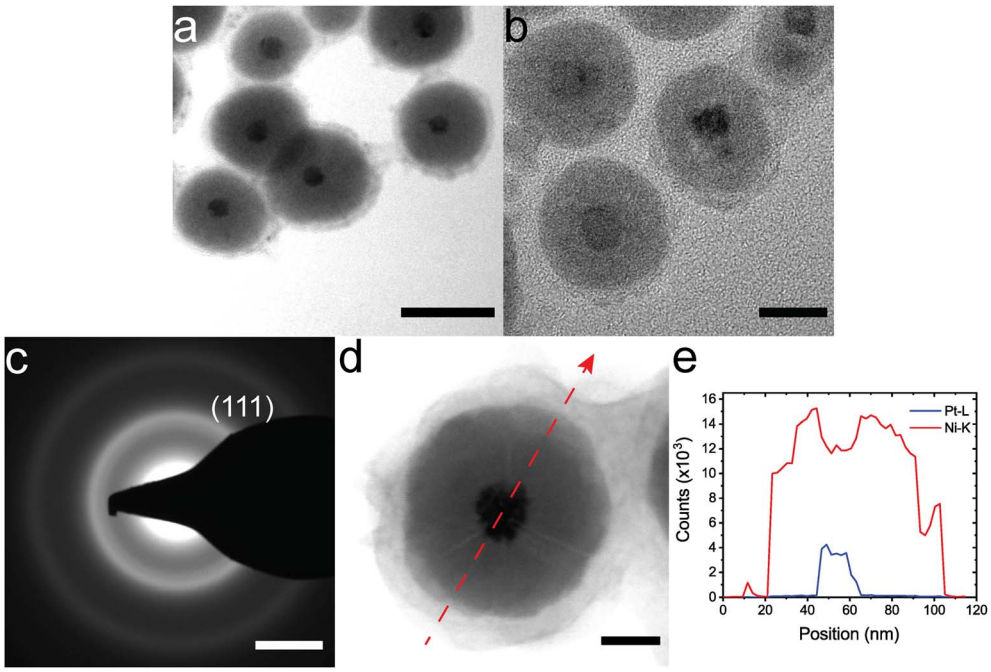

Fig. 2 (a) Citrate-Au@CoB nanoparticles. Scale bar is 50 nm. (b) 5 nm Pt nanoparticles with 5 nm thick coating. Scale bar is 10 nm. (c) Selected area diffraction pattern for 5 nm Pt nanoparticles with 5 nm thick NiB coating. Scale bar is 4 nm^{-1}. (d) 20 nm Pt nanocrystal with 25 nm thick NiB coating. Arrow denotes direction of STEM-EDS line scan. Scale bar is 20 nm. (e) Intensity profile of STEM-EDS scan for Pt-L and Ni–K peaks.

citrate-Au@NiB nanoparticles and 3.16 $Å^{-1}$ for NiB nanoparticles. This indicates that the shell on the citrate-Au core is stretched under tensile forces, which we attribute to the surface curvature of the core nanoparticle. The citrate–Au core XRD peaks match with the bulk Au peak positions and the observed peak broadening is due to the small nanoparticle size. Fig. 3b shows the *in situ* XRD high pressure compression of citrate-Au@NiB core–shell nanoparticles. The nanoparticles were compressed from 0.6 GPa to 55 GPa under quasi-hydrostatic loading. The XRD peaks for Au core are present throughout the pressure range, and the peaks shift towards the right with increasing pressure indicating the lattice compression for Au core. The amorphous XRD peaks for NiB were overlapping with the Au crystalline peaks. The NiB coating stays amorphous up to 55 GPa pressure.

Fig. 3c shows that the plasmon resonance of citrate-Au nanoparticles has a peak around ~530 nm. The plasmon resonance of the Au core nanoparticle is severely dampened after coating with the NiB shell. The plasmon peak width increases after the additional of the shell coating and the peak intensity drops with increasing thickness of the NiB shell, but the energy of the peak does not shift (Fig. 3c). The dampened plasmon resonance of citrate-Au@NiB nanoparticles can still be used for applications in biomedicine, photonics and as a pressure marker for high-pressure experiments.[51–54]

The magnetic properties of coated Au nanoparticles were investigated. Previous experimental results have shown that pure NiB[55] and CoB[23] amorphous particles are paramagnetic and ferromagnetic, respectively. The citrate-Au@NiB from Fig. 1c and the citrate-Au@CoB from Fig. 2a were used for

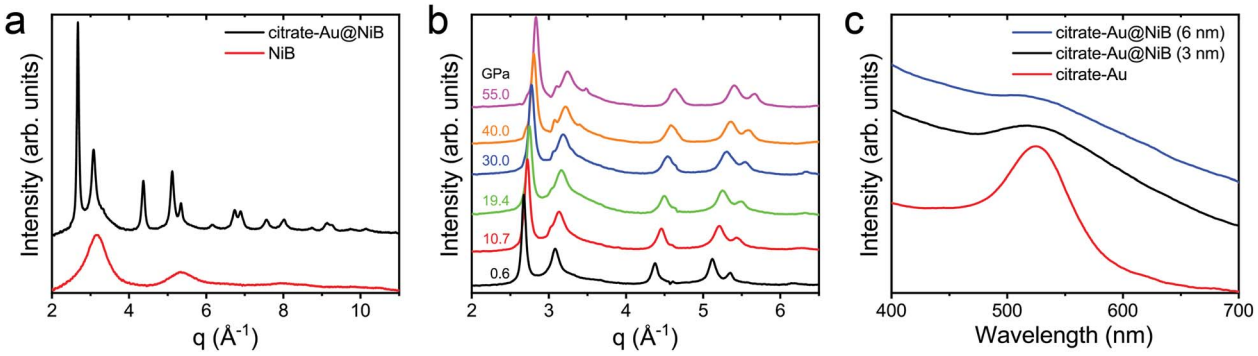

Fig. 3 (a) XRD of citrate-Au@NiB and amorphous NiB nanoparticles. (b) XRD curves of citrate-Au@NiB under pressure. (c) Absorbance spectra of bare and coated citrate–Au nanoparticles with 3 and 6 nm shell thickness.

magnetic studies. Citrate-Au@CoB nanoparticles exhibit ferromagnetic behavior that persists up to room temperature. Fig. 4a shows hysteresis in the field dependence of the magnetization with finite remanence up to 300 K. The temperature dependence of the magnetization shown in Fig. 4c suggests a magnetic transition temperature above room temperature. Citrate-Au@NiB nanoparticles show transitions from ferromagnetic to superparamagnetic to paramagnetic across the temperature range 5–300 K. At low temperatures, the citrate Au@NiB nanoparticles exhibit ferromagnetic behavior with hysteretic field dependent magnetization loops (Fig. 4b). As field dependent magnetization is measured at higher temperatures, we observe the onset of superparamagnetism and eventually weak paramagnetism at 300 K along with a diamagnetic background signal from the Si substrate. In order to determine the onset temperature of superparamagnetism, we measure the sample in 500 Oe after it has been cooled in a strong magnetic field of 1 T as well as in 500 Oe after being cooled in zero magnetic field. Temperature dependences of the field cooled (FC) and zero field cooled (ZFC) magnetization (Fig. 4d) deviate from each other at 12 K, where there is a maximum in the ZFC magnetization signal. The deviation of the FC and ZFC curves can be correlated with the onset of superparamagnetism and blocking temperature of $T_B = 12$ K. Below T_B, the ZFC magnetization of nanoparticles is effectively frozen in random orientations, while the FC magnetization of the nanoparticles is aligned. The blocking temperature of 12 K observed in the NiB nanoparticles is consistent with other findings that report a blocking temperature of 14 K for amorphous NiB nanoparticles.[40]. This is well below the transition temperature observed for the CoB core shell nanoparticles, which exhibit a T_C above room temperature.

In summary, we have demonstrated a versatile metallic glass coating for nanoparticles synthesized in aqueous solution. Coating thickness can be precisely controlled by varying the nanoparticle concentration. The coating thickness has low variation above a thickness of 5 nm. These coatings are chemically stable, radiation resistant, and para/ferromagnetic. The synthesis strategy is universal for different core sizes, shapes, and compositions, and could easily be extended to other aqueous nanoparticle cores such Pd, Cu, Fe_3O_4 and CdSe.[56–59] The aqueous phase shell synthesis limits the use of air and moisture sensitive nanoparticles as the crystalline core. The synthesis is limited to aqueous phase nanoparticles capped with short molecular weight and low binding energy ligands. The presence of a ligand, CTAC or citric acid, or underlying

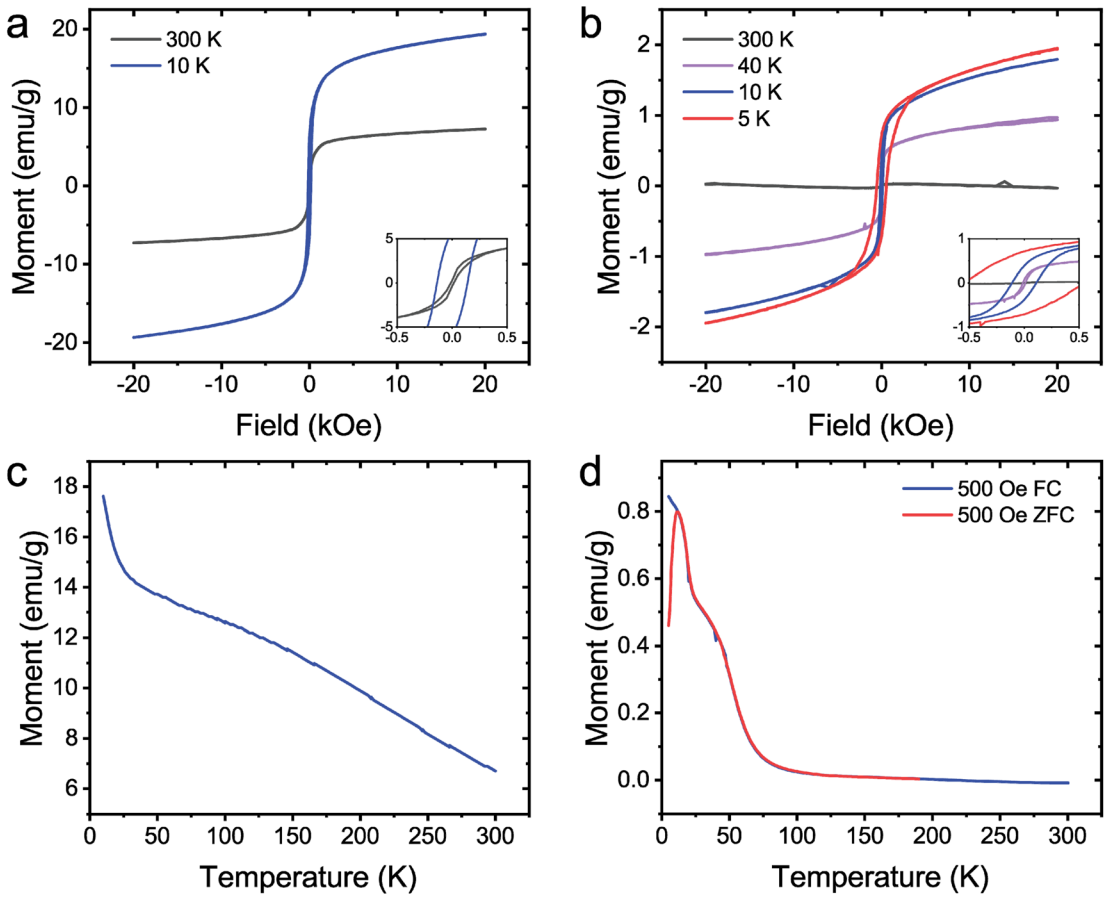

Fig. 4 (a) Magnetization of citrate-Au@CoB nanoparticles at 10 K and 300 K. (b) Magnetization of citrate-Au@NiB nanoparticles at 5, 10, 40, and 300 K. Insets for (a) and (b) show moment near 0 Oe. (c) Temperature-dependent magnetic moment at 1 T for citrate-Au@CoB. (d) Temperature-dependent magnetic moment at 1 T for citrate-Au@NiB.

nanoparticle metal, Au or Pt, did not affect the coating synthesis and future work could expand the synthesis strategy to more nanoparticle metal/ligands. Coating compositions could be extended to other amorphous metal borides, *e.g.* FeB.

Conflicts of interest

There are no conflicts of interest to declare.

Acknowledgements

We thank Guoyin Shen and Sergey N. Tkachev for assistance with remote high-pressure beamline experiments. We gratefully acknowledge financial support from the grant DE-SC0021075 funded by the U.S. Department of Energy, Office of Science. E. L. and Y. S. acknowledge support from NSF Award No. 2037652. Part of this work was performed at the Stanford Nano Shared Facilities (SNSF), supported by the National Science Foundation under award ECCS-1542152. A. C. L. is supported by Knight-Hennessy Scholars. M. T. K. acknowledges the National Defense and Science Engineering Graduate Fellowship. Portions of this work were performed at HPCAT (Sector 16), Advanced Photon Source (APS), Argonne National Laboratory. HPCAT operations are supported by DOE-NNSA's Office of Experimental Sciences. The Advanced Photon Source is a U.S. Department of Energy (DOE) Office of Science User Facility operated for the DOE Office of Science by Argonne National Laboratory under Contract No. DE-AC02-06CH11357. LLNL review and release number LLNL-JRNL-844066-DRAFT. This work was performed under the auspices of the U.S. Department of Energy by Lawrence Livermore National Laboratory under Contract DE-AC52-07NA27344. Use of the COMPRES-GSECARS gas loading system was supported by COMPRES under NSF Cooperative Agreement EAR-1606856 and by GSECARS through NSF grant EAR-1634415 and DOE grant DE-FG02-94ER14466.

References

1 Y. Xia, Y. Xiong, B. Lim and S. E. Skrabalak, Shape-Controlled Synthesis of Metal Nanocrystals: Simple Chemistry Meets Complex Physics?, *Angew. Chem., Int. Ed.*, 2009, **48**(1), 60–103, DOI: **10.1002/anie.200802248**.

2 K. Chatterjee, S. Sarkar, K. Jagajjanani Rao and S. Paria, Core/Shell Nanoparticles in Biomedical Applications, *Adv. Colloid Interface Sci.*, 2014, **209**, 8–39, DOI: **10.1016/j.cis.2013.12.008**.

3 M. B. Gawande, A. Goswami, T. Asefa, H. Guo, A. V. Biradar, D. L. Peng, R. Zboril and R. S. Varma, Core-Shell Nanoparticles: Synthesis and Applications in Catalysis and Electrocatalysis, *Chem. Soc. Rev.*, 2015, **7**, 7540–7590, DOI: **10.1039/c5cs00343a**.

4 Y. Wu, P. Jiang, M. Jiang, T. W. Wang, C. F. Guo, S. S. Xie and Z. L. Wang, The Shape Evolution of Gold Seeds and Gold@silver Core-Shell Nanostructures, *Nanotechnology*, 2009, **20**(30), 305602, DOI: **10.1088/0957-4484/20/30/305602**.

5 J. Zhang, Y. Tang, K. Lee and M. Ouyang, Nonepitaxial Growth of Hybrid Core-Shell Nanostructures with Large Lattice Mismatches, *Science*, 2010, **327**(5973), 1634–1638, DOI: **10.1126/science.1184769**.

6 B. D. Anderson and J. B. Tracy, Nanoparticle Conversion Chemistry: Kirkendall Effect, Galvanic Exchange, and Anion Exchange, *Nanoscale*, 2014, 12195–12216, DOI: **10.1039/c4nr02025a**.

7 R. Ghosh Chaudhuri and S. Paria, Core/Shell Nanoparticles: Classes, Properties, Synthesis Mechanisms, Characterization, and Applications, *Chem. Rev.*, 2012, **112**(4), 2373–2433, DOI: **10.1021/cr100449n**.

8 C. Ma, B. Luo, H. H. Song and L. J. Zhi, Preparation of Carbon-Encapsulated Metal Magnetic Nanoparticles by an Instant Pyrolysis Method, *N. Carbon Mater.*, 2010, **25**(3), 199–204, DOI: **10.1016/S1872-5805(09)60028-7**.

9 Q. Barati and S. M. M. Hadavi, Electroless Ni-B and Composite Coatings: A Critical Review on Formation Mechanism, Properties, Applications and Future Trends, *Surface. Interfac.*, 2020, **1**, 100702, DOI: **10.1016/j.surfin.2020.100702**.

10 J. R. Scully, A. Gebert and J. H. Payer, Corrosion and Related Mechanical Properties of Bulk Metallic Glasses, *J. Mater. Res.*, 2007, 302–313, DOI: **10.1557/jmr.2007.0051**.

11 S. Gupta, M. K. Patel, A. Miotello and N. Patel, Metal Boride-Based Catalysts for Electrochemical Water-Splitting: A Review, *Adv. Funct. Mater.*, 2020, **30**(1), 1906481, DOI: **10.1002/adfm.201906481**.

12 S. Dutta, H. S. Han, M. Je, H. Choi, J. Kwon, K. Park, A. Indra, K. M. Kim, U. Paik and T. Song, Chemical and Structural Engineering of Transition Metal Boride towards Excellent and Sustainable Hydrogen Evolution Reaction, *Nano Energy*, 2020, **67**, 104245, DOI: **10.1016/j.nanoen.2019.104245**.

13 S. Gupta, N. Patel, A. Miotello and D. C. Kothari, Cobalt-Boride: An Efficient and Robust Electrocatalyst for Hydrogen Evolution Reaction, *J. Power Sources*, 2015, **279**, 620–625, DOI: **10.1016/j.jpowsour.2015.01.009**.

14 D. He, L. Zhang, D. He, G. Zhou, Y. Lin, Z. Deng, X. Hong, Y. Wu, C. Chen and Y. Li, Amorphous Nickel Boride Membrane on a Platinum-Nickel Alloy Surface for Enhanced Oxygen Reduction Reaction, *Nat. Commun.*, 2016, **7**(1), 1–8, DOI: **10.1038/ncomms12362**.

15 D. Hua, Y. Hanxi, A. Xinping and C. Chuansin, Hydrogen Production from Catalytic Hydrolysis of Sodium Borohydride Solution Using Nickel Boride Catalyst, *Int. J. Hydrogen Energy*, 2003, **28**(10), 1095–1100, DOI: **10.1016/S0360-3199(02)00235-5**.

16 U. B. Demirci and P. Miele, Cobalt-Based Catalysts for the Hydrolysis of NaBH4 and NH 3BH3, *Phys. Chem. Chem. Phys.*, 2014, **21**, 6872–6885, DOI: **10.1039/c4cp00250d**.

17 J. Manna, B. Roy, D. Pareek and P. Sharma, Hydrogen Generation from NaBH4 Hydrolysis Using Co-B/AlPO4 and Co-B/Bentonite Catalysts, *Catal. Struct. React.*, 2017, **3**(4), 157–164, DOI: **10.1080/2055074X.2017.1344793**.

18 J. Masa, P. Weide, D. Peeters, I. Sinev, W. Xia, Z. Sun, C. Somsen, M. Muhler and W. Schuhmann, Amorphous Cobalt Boride (Co 2 B) as a Highly Efficient Nonprecious Catalyst for Electrochemical Water Splitting: Oxygen and

Hydrogen Evolution, *Adv. Energy Mater.*, 2016, **6**(6), 1502313, DOI: 10.1002/aenm.201502313.

19 C. C. Wang, S. A. Akbar, W. Chen and V. D. Patton, Electrical Properties of High-Temperature Oxides, Borides, Carbides, and Nitrides, *J. Mater. Sci.*, 1995, **13**, 1627–1641, DOI: 10.1007/BF00351591.

20 M. T. Kiani, C. M. Barr, S. Xu, D. Doan, Z. Wang, A. Parakh, K. Hattar and X. W. Gu, Ductile Metallic Glass Nanoparticles via Colloidal Synthesis, *Nano Lett.*, 2020, **20**(9), 6481–6487, DOI: 10.1021/acs.nanolett.0c02177.

21 A. Parakh, M. T. Kiani, A. Colmenares, A. C. Lee, S. Chariton, V. Prakapenka and X. W. Gu, High-pressure deformation of metallic glass nanoparticles, *J. Non-Cryst. Solids*, 2022, **597**, 121923, DOI: 10.1016/j.jnoncrysol.2022.121923.

22 M. M. Wang, M. T. Kiani, A. Parakh, Y. Jiang and X. W. Gu, Effect of grain size on iron-boride nanoglasses, *J. Mater. Sci. Technol.*, 2023, **141**, 116–123, DOI: 10.1016/j.jmst.2022.09.025.

23 A. B. Dávila-Ibáñez, J. L. Legido-Soto, J. Rivas and V. Salgueirino, Amorphous Tunable-Size Co-B Magnetic Nanoparticles from the Cobalt-Catalyzed NaBH4 Hydrolysis, *Phys. Chem. Chem. Phys.*, 2011, **13**(45), 20146–20154, DOI: 10.1039/c1cp21988j.

24 V. Torresan, A. Guadagnini, D. Badocco, P. Pastore, G. A. Muñoz Medina, M. B. Fernàndez van Raap, I. Postuma, S. Bortolussi, M. Bekić, M. Čolić, M. Gerosa, A. Busato, P. Marzola and V. Amendola, Biocompatible Iron–Boron Nanoparticles Designed for Neutron Capture Therapy Guided by Magnetic Resonance Imaging, *Adv. Healthc. Mater.*, 2021, **10**(6), 2001632, DOI: 10.1002/adhm.202001632.

25 H. Türkez, M. E. Arslan, E. Sönmez, A. Tatar, F. Geyikoğlu, M. Açikyildiz and A. Mardinoğlu, Safety Assessments of Nickel Boride Nanoparticles on the Human Pulmonary Alveolar Cells by Using Cell Viability and Gene Expression Analyses, *Biol. Trace Elem. Res.*, 2021, **199**(7), 2602–2611, DOI: 10.1007/s12011-020-02374-7.

26 M. T. Kiani, K. Hattar and X. W. Gu, In Situ TEM Study of Radiation Resistance of Metallic Glass-Metal Core-Shell Nanocubes, *ACS Appl. Mater. Interfaces*, 2020, **12**(36), 40910–40916, DOI: 10.1021/acsami.0c10664.

27 V. Amendola, S. Scaramuzza, L. Litti, M. Meneghetti, G. Zuccolotto, A. Rosato, E. Nicolato, P. Marzola, G. Fracasso, C. Anselmi, M. Pinto and M. Colombatti, Magneto-Plasmonic Au-Fe Alloy Nanoparticles Designed for Multimodal SERS-MRI-CT Imaging, *Small*, 2014, **10**(12), 2476–2486, DOI: 10.1002/smll.201303372.

28 Y. Zheng, X. Zhong, Z. Li and Y. Xia, Successive, Seed-Mediated Growth for the Synthesis of Single-Crystal Gold Nanospheres with Uniform Diameters Controlled in the Range of 5-150 Nm, *Part. Part. Syst. Char*, 2014, **31**(2), 266–273, DOI: 10.1002/ppsc.201300256.

29 N. G. Bastús, J. Comenge and V. Puntes, Kinetically Controlled Seeded Growth Synthesis of Citrate-Stabilized Gold Nanoparticles of up to 200 Nm: Size Focusing versus Ostwald Ripening, *Langmuir*, 2011, **27**(17), 11098–11105, DOI: 10.1021/la201938u.

30 N. C. Bigall, T. Härtling, M. Klose, P. Simon, L. M. Eng and A. Eychmüller, Monodisperse Platinum Nanospheres with Adjustable Diameters from 10 to 100 Nm: Synthesis and Distinct Optical Properties, *Nano Lett.*, 2008, **8**(12), 4588–4592, DOI: 10.1021/nl802901t.

31 G. Shen, Y. Wang, A. Dewaele, C. Wu, D. E. Fratanduono, J. Eggert, S. Klotz, K. F. Dziubek, P. Loubeyre, O. V. Fat'yanov, P. D. Asimow, T. Mashimo and R. M. M. Wentzcovitch, Toward an International Practical Pressure Scale: A Proposal for an IPPS Ruby Gauge (IPPS-Ruby2020), *High Press. Res.*, 2020, 299–314, DOI: 10.1080/08957959.2020.1791107.

32 C. Prescher and V. B. Prakapenka, DIOPTAS: A Program for Reduction of Two-Dimensional X-Ray Diffraction Data and Data Exploration, *High Press. Res.*, 2015, **35**(3), 223–230, DOI: 10.1080/08957959.2015.1059835.

33 A. Rinaldi, S. Licoccia, E. Traversa, K. Sieradzki, P. Peralta, A. B. Dávila-Ibáñez, M. A. Correa-Duarte and V. Salgueirino, Radial Inner Morphology Effects on the Mechanical Properties of Amorphous Composite Cobalt Boride Nanoparticles, *J. Phys. Chem. C*, 2010, **114**(32), 13451–13458, DOI: 10.1021/jp102560c.

34 L. J. E. Hofer, J. F. Shultz, R. D. Panson and R. B. Anderson, The Nature of the Nickel Boride Formed by the Action of Sodium Borohydride on Nickel Salts, *Inorg. Chem.*, 1964, 1783–1785, DOI: 10.1021/ic50022a031.

35 Y. Peng, Q. Chen, J. Xie and W. Lan, Communication—Facile Synthesis of Amorphous Nickel Boride Nanoparticles for Highly Sensitive Non-Enzyme Glucose Detection, *J. Electrochem. Soc.*, 2019, **166**(6), B521–B523, DOI: 10.1149/2.1321906jes.

36 P. Chen, S. Zhang, Y. Fan, W. Yang and X. Luo, Constructing Amorphous/Amorphous Heterointerfaces in Nickel Borate/Boride Composites for Efficient Electrocatalytic Methanol Oxidation, *Mater. Adv.*, 2023, **4**(5), 1363–1371, DOI: 10.1039/d2ma01037b.

37 R. Chen, L. Liu, J. Zhou, L. Hou and F. Gao, High-Performance Nickel-Cobalt-Boron Material for an Asymmetric Supercapacitor with an Ultrahigh Energy Density, *J. Power Sources*, 2017, **341**, 75–82, DOI: 10.1016/j.jpowsour.2016.11.108.

38 W. Li, S. Wang, M. Wu, X. Wang, Y. Long and X. Lou, Direct Aqueous Solution Synthesis of an Ultra-Fine Amorphous Nickel-Boron Alloy with Superior Pseudocapacitive Performance for Advanced Asymmetric Supercapacitors, *New J. Chem.*, 2017, **41**(15), 7302–7311, DOI: 10.1039/c7nj00222j.

39 T. Tan, P. Han, H. Cong, G. Cheng and W. Luo, An Amorphous Cobalt Borate Nanosheet-Coated Cobalt Boride Hybrid for Highly Efficient Alkaline Water Oxidation Reaction, *ACS Sustain. Chem. Eng.*, 2019, **7**(6), 5620–5625, DOI: 10.1021/acssuschemeng.9b00258.

40 J. F. Hou, J. F. Gao and L. Bin Kong, Liquid Phase Reduction Synthesis of a Cobalt Boride-Activated Carbon Composite with Improved Specific Capacitance and Retention Rate as a New Positive Electrode Material for Supercapacitors, *New*

J. Chem., 2019, **43**(36), 14475–14484, DOI: **10.1039/c9nj02830g**.

41 J. Legrand, A. Taleb, S. Gota, M. J. Guittet and C. Petit, Synthesis and XPS Characterization of Nickel Boride Nanoparticles, *Langmuir*, 2002, **18**(10), 4131–4137, DOI: **10.1021/la0117247**.

42 L. D. Van Ee, B. J. Thijsse and J. Sietsma, Evidence for Two-Level States and Cooperative Atomic Jumps in a Computer Model of Amorphous Ni81B19, *Mater. Sci. Eng. A*, 1997, **226**, 228, DOI: **10.1016/s0921-5093(96)10633-x**.

43 E. W. Iparraguirre, J. Sietsma, B. J. Thijsse and L. Pusztai, A Reverse Monte Carlo Study of Amorphous Ni81B19, *Comput. Mater. Sci.*, 1993, **1**(2), 110–122, DOI: **10.1016/0927-0256(93)90002-5**.

44 P. Lamparter, W. Sperl, S. Steeb and J. Bletry, Atomic Structure of Amorphous Metallic Ni81B19, *Z. Naturforsch., A*, 1982, **37**(11), 1223–1234, DOI: **10.1515/zna-1982-1102**.

45 H. W. Sheng, W. K. Luo, F. M. Alamgir, J. M. Bai and E. Ma, Atomic Packing and Short-to-Medium-Range Order in Metallic Glasses, *Nature*, 2006, **439**(7075), 419–425, DOI: **10.1038/nature04421**.

46 L. Pusztai and E. Svab, Modelling the Structure of Ni65B35 Metallic Glass by Reverse Monte Carlo Simulation, *J. Phys.: Condens. Matter*, 1993, **5**, 8815, DOI: **10.1088/0953-8984/5/47/007**.

47 P. Lamparter, Reverse Monte Carlo Simulation of Amorphous Ni80p20 and Ni81b19, *Phys. Scr.*, 1995, **1995**(T57), 72–78, DOI: **10.1088/0031-8949/1995/T57/011**.

48 S. Liu and M.-Y. Han, Silica-Coated Metal Nanoparticles, *Chem.–Asian J.*, 2009, **5**(1), 36–45, DOI: **10.1002/asia.200900228**.

49 L. M. Liz-Marzán, M. Giersig and P. Mulvaney, Synthesis of Nanosized Gold-Silica Core-Shell Particles, *Langmuir*, 1996, **12**(18), 4329–4335, DOI: **10.1021/la9601871**.

50 A. A. Taskin, F. Yang, S. Sasaki, K. Segawa and Y. Ando, Topological Surface Transport in Epitaxial SnTe Thin Films Grown on Bi2Te3, *Phys. Rev. B*, 2013, **89**, 121302, DOI: **10.1103/PhysRevB.89.121302**.

51 L. Wang, M. Hasanzadeh Kafshgari and M. Meunier, Optical Properties and Applications of Plasmonic-Metal Nanoparticles, *Adv. Funct. Mater.*, 2020, **30**(2005400), DOI: **10.1002/adfm.202005400**.

52 J. H. Lee, H. Y. Cho, H. K. Choi, J. Y. Lee and J. W. Choi, Application of Gold Nanoparticle to Plasmonic Biosensors, *Int. J. Mol. Sci.*, 2018, **19**(7), DOI: **10.3390/ijms19072021**.

53 X. W. Gu, L. A. Hanson, C. N. Eisler, M. A. Koc and A. P. Alivisatos, Pseudoelasticity at Large Strains in Au Nanocrystals, *Phys. Rev. Lett.*, 2018, **121**(5), 056102, DOI: **10.1103/PhysRevLett.121.056102**.

54 A. Parakh, S. Lee, K. A. Harkins, M. T. Kiani, D. Doan, M. Kunz, A. Doran, L. A. Hanson, S. Ryu and X. W. Gu, Nucleation of Dislocations in 3.9 Nm Nanocrystals at High Pressure, *Phys. Rev. Lett.*, 2020, **124**(10), 106104, DOI: **10.1103/PhysRevLett.124.106104**.

55 D. S. Sidhaye, T. Bala, S. Srinath, H. Srikanth, P. Poddar, M. Sastry and B. L. V. Prasad, Preparation of Nearly Monodisperse Nickel Nanoparticles by a Facile Solution Based Methodology and Their Ordered Assemblies, *J. Phys. Chem. C*, 2009, **113**(9), 3426–3429, DOI: **10.1021/jp807542w**.

56 Y. Piao, Y. Jang, M. Shokouhimehr, I. S. Lee and T. Hyeon, Facile Aqueous-Phase Synthesis of Uniform Palladium Nanoparticles of Various Shapes and Sizes, *Small*, 2007, **3**(2), 255–260, DOI: **10.1002/smll.200600402**.

57 Y. S. Park, A. Dmytruk, I. Dmitruk, A. Kasuya, Y. Okamoto, N. Kaji, M. Tokeshi and Y. Baba, Aqueous Phase Synthesized CdSe Nanoparticles with Well-Defined Numbers of Constituent Atoms, *J. Phys. Chem. C*, 2010, **114**(44), 18834–18840, DOI: **10.1021/jp107608b**.

58 Y. Kamikoriyama, H. Imamura, A. Muramatsu and K. Kanie, Ambient Aqueous-Phase Synthesis of Copper Nanoparticles and Nanopastes with Low-Temperature Sintering and Ultra-High Bonding Abilities, *Sci. Rep.*, 2019, **9**(1), 1–10, DOI: **10.1038/s41598-018-38422-5**.

59 J. Li, S. Wang, X. Shi and M. Shen, Aqueous-Phase Synthesis of Iron Oxide Nanoparticles and Composites for Cancer Diagnosis and Therapy, *Adv. Colloid Interface Sci.*, 2017, **1**, 374–385, DOI: **10.1016/j.cis.2017.02.009**.